**Article**

# Strong impact of the rare three-year La Niña event on Antarctic surface climate changes in 2021–2023

Check for updates

Shaoyin Wang[1,2] ✉, Jiping Liu[2,3] ✉, Wenju Cai[4], Dongxia Yang[5], Tobias Kerzenmacher[6], Suoyi Ding[7] & Xiao Cheng[1,2]

From 2021 to 2023, satellite records reveal that February Antarctic sea ice extent reached record lows in 2022 and 2023. Simultaneously, the Antarctic ice sheet experienced a transient mass gain and rebounded temporarily from a decadal decline since 2002. The reasons behind these dramatic changes are unknown. Here, we show that the triple-dip La Niña event during 2021–2023 (referred to as TD_LN2023) played a major role in these changes. Compared to a previous triple-dip La Niña event (1999–2001), the tropical-Antarctic teleconnections during TD_LN2023 were stronger. A more pronounced southward shift of the Ferrel Cell was identified as a key driver for the enhanced tropical-Antarctic teleconnections during TD_LN2023 against the background of intensified westerly winds and tropical expansion. The poleward increase, which facilitated poleward atmospheric heat and moisture transport, contributed to the sea ice extent decline and the ice sheet mass growth. Additionally, this southward shift strengthened the Rossby wave train, which, sustained by enhanced stratosphere-troposphere coupling, amplified the Pacific-South American pattern, and further promoted regional sea ice decline. Finally, this southward shift, associated with the southward shift of the westerly jet, enhanced Ekman suction, bringing subsurface warm water to the surface and contributing to pan-Antarctic low sea ice. The physical processes outlined in the case study are further validated through empirical orthogonal function and regression analysis. Under global warming, multi-year La Niña events are projected to occur more frequently. The evolving tropical-Antarctic teleconnections in the context warrant close attention.

Warming in the Antarctic and its surrounding Southern Ocean is slower compared to that over many regions, such as, the Arctic, where rapid warming has been observed. Unlike the Arctic, Antarctica has not experienced substantial large-scale warming[1]. Furthermore, Antarctic sea ice exhibits a more complex evolution pattern compared to the near-monotonic decline of Arctic sea ice[2,3]. This disparity between the Arctic and Antarctic is partly due to a substantial heat uptake by the Southern Ocean, which delays the surface warming in this region[4].

However, in recent years, abrupt surface changes across Antarctica have emerged, with hotspots developing over both the Antarctic continent and the Southern Ocean, signaling a profound shift in the Antarctic climate[5–8]. Firstly, from 2021 to 2023, annual (average from July through June of the following year) sea ice extent (SIE) continued to decline, reaching a record low in 2023 (Fig. 1a), with annual (February) SIE about 10.39 (1.91) million km$^2$ in 2023[5,9]. In 2023, annual (February) SIE decreased by approximately 11% (38%) compared to the climatological mean (Fig. S1a). Two satellite-retrieved datasets confirm the pronounced decline in sea ice from 2021 to 2023 (Fig. 1a). Regionally, substantial sea ice reductions

[1]School of Geospatial Engineering and Science, Sun Yat-sen University, and Southern Marine Science and Engineering Guangdong Laboratory (Zhuhai), Zhuhai, China. [2]Key Laboratory of Comprehensive Observation of Polar Environment (Sun Yat-sen University), Zhuhai, China. [3]School of Atmospheric Sciences, Sun Yat-sen University and Southern Marine Science and Engineering Guangdong Laboratory (Zhuhai), Zhuhai, China. [4]Frontiers Science Center for Deep Ocean Multispheres and Earth System (FDOMES) and Key Laboratory of Physical Oceanography, Ocean University of China, Qingdao, China. [5]Analycia Pty. Ltd, Melbourne, VIC, Australia. [6]Karlsruhe Institute of Technology (KIT), Institute of Meteorology and Climate Research Atmospheric Trace Gases and Remote Sensing (IMKASF), Karlsruhe, Germany. [7]Department of Atmospheric and Oceanic Sciences, Fudan University, Shanghai, China. ✉e-mail: wangshy96@mail.sysu.edu.cn; liujp63@mail.sysu.edu.cn
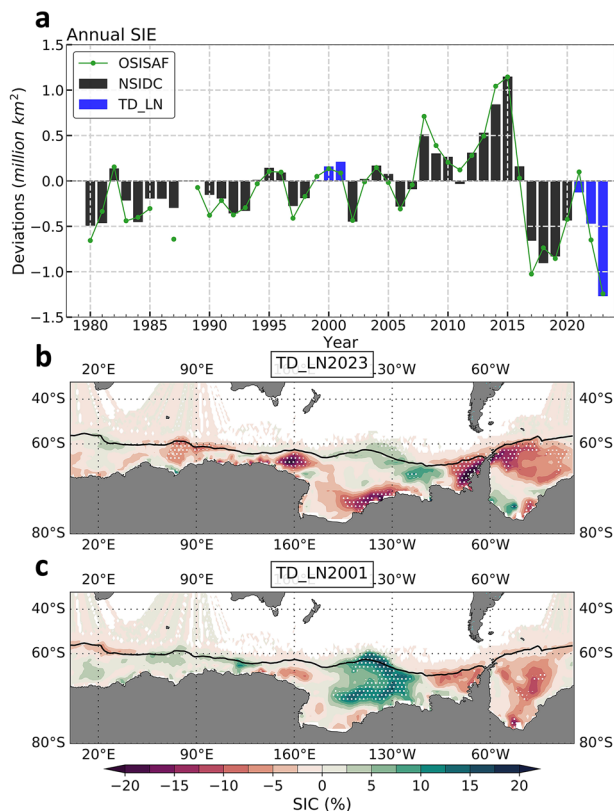
**Fig. 1 | Dramatic decrease in Antarctic sea ice during the recent triple-dip La Niña event compared to 1999–2001. a** Timeseries of annual Sea Ice Extent (SIE) from 1980–2023 (black bar: NSIDC with TD_LN years highlighted in blue; green line: OSISAF). **b, c** Annual Sea Ice Concentration (SIC) anomalies averaged over 2021–2023 and 1999–2001, respectively, relative to the 1991–2020 climatology. The dots indicate where the SIC anomalies exceed one standard deviation ($1\sigma$) of the climatology (1991–2020). Black lines in (**b, c**) represent the climatological sea ice edges (15% SIC).

(exceeding 20% sea ice concentration, SIC) were observed in eastern Ross Sea, northern Weddell Sea, and along the eastern Antarctic coastline, with anomalies exceeding one standard deviation ($1\sigma$) (Fig. 1b and Fig. S1b). During a previous triple-dip La Niña event (referred to as TD_LN2001), Antarctic SIE remained within a normal range, with an averaged annual (February) SIE around 11.79 (3.0) million km², highlighting a sharp contrast to that observed in TD_LN2023.

Secondly, the Antarctic ice sheet (AIS) mass experienced a notable increase from 2021 to 2023, temporarily rebounding from a decadal decline since 2002 (Fig. 2a). During 2003–2023, the total AIS mass from 2003 to 2021 showed a continuous decrease. However, in 2022, a temporary rebound occurred, with an increase of approximately 205.43 Gt (relative to 2020–2021), equivalent to a global mean sea level change about 0.55 mm. The AIS mass changes result from a combination of surface mass balance (SMB) and ice dynamic processes[10]. The SMB consists of total precipitation, sublimation and runoff, while the ice dynamic processes are mainly related to ice discharge across the grounding line[10]. Due to discrepancies in discharge estimated from different studies[11–13], only the SMB data from the RACMO2.4P1 is applied to analyze the cumulative mass changes. Overall, beginning around 2007, the cumulative SMB anomaly exhibits a continuous decline but shows a substantially increase from approximately 2020, particularly in 2022 (Fig. 2b). This pattern closely aligns with the evolution of the AIS mass changes observed from 2021 to 2023 (Fig. 2a), indicating that the cumulative SMB changes are vital for the AIS mass gain during TD_LN2023. The spatial pattern of the SMB anomalies during this period show a substantial increase along the sea ice edges, particularly in the Bellingshausen Sea, and along the Antarctic coasts, most notably on the eastern

side (Fig. 2c). Simultaneously, the total precipitation anomalies (i.e., snowfall plus rainfall) closely resemble the SMB anomalies (Fig. 2d), indicating that increased precipitation in TD_LN2023 dominated the SMB changes, which, in turn, contributed to the temporary rise in AIS mass. Recent studies[8,14] also suggested that the rise in East Antarctic surface mass is largely attributed to greater snowfall accumulation.

These anomalous events coincided with a three consecutive La Niña during TD_LN2023 (Figs. S2–3). A strong connection exists between tropical Pacific sea surface temperature (SST) and Antarctic surface climate[15–18]. A pathway is that the El Niño and Southern Oscillation (ENSO) drives large-scale atmospheric Rossby waves that propagate poleward along great circles[19], forming the Pacific Southern American (PSA) mode. The PSA mode is a pattern characterized by anomaly centers east of New Zealand, in the Amundsen-Bellingshausen Sea, and the northern Weddell Sea[20]. However, whether the substantial Antarctic surface climate changes (i.e., sea ice and ice sheet mass changes) during TD_LN2023 are dynamically linked to the prolonged La Niña event is still unknown.

Below, we explore dynamics behind the dramatic changes in Antarctic sea ice and ice sheet from the perspective of tropical-Antarctic teleconnections. We find that the rare three-year La Niña event had an enhanced impact on Antarctic surface climate changes from 2021 to 2023, primarily through a pronounced southward shift of the Ferrel Cell and the associated circulation changes from 2021 to 2023.

## Results

### Southward shift of the Ferrel Cell during 2021–2023

The Ferrel Cell is characterized by ascent of relatively cold air in high latitudes and the descent of relatively warm air in lower mid-latitudes[21]. It plays a crucial role in the poleward transport of heat and moisture, influencing mid- to high- latitude weather and climate patterns[22–24]. In TD_LN2023, the meridional mass stream function (MSF) shows a substantial intensification of the Ferrel Cell, with a magnitude of approximately $6 \times 10^9$ kg/sec (Fig. 3a). Compared to its climatological position, the MSF in TD_LN2023 shifted southward. The strengthening and southward shift of the Ferrel Cell is accompanied by an ascent branch over latitudes 55–70°S and a descending branch over mid-latitudes (40–55°S), corresponding to a mid-latitude warming of approximately 1 K (Fig. 3b). The mid-latitude atmospheric warming enhances the meridional temperature gradient between the mid- and high-latitudes (Fig. 3b), which, in turn, causes a southward shift of the westerly jet from the surface to the upper troposphere (50–70°S), in accordance with the thermal wind relationship (Fig. 3c). The poleward shift of the westerly jet and temperature anomalies largely resemble the positive phase of the Southern Annular Mode (SAM)[25]. In contrast, the Ferrel Cell and jet stream anomalies during TD_LN2001 were located further north and weaker than those observed in TD_LN2023 (Fig. 3e–g vs. Fig. 3a–c).

The southward shift of the Ferrel Cell during TD_LN2023 is also accompanied by the southward transport and, more importantly, the convergence of moist static energy (MSE, Fig. 3d); the intensified advection of heat and moisture (also compared that during TD_LN2001, Fig. 3d vs. h), particularly their convergence towards the sea ice regions (60–70°S), contributed to the low Antarctic sea ice during TD_LN2023. Consistently, the precipitation anomalies during TD_LN2023 were centered between 50°S and 70°S, exceeding $1\sigma$, aligning and coherent with the increased moisture convergence in this region (Fig. 4a). Similarly, the substantial increase of the net surface heat flux (Qnet) by approximately 2 W/m² is consistent with convergence of MSE over the latitude band from ~55°S to 70°S (Fig. 4b), contributing to the low level of SIE. Notably, the increase in Qnet is largely attributed to enhanced downward longwave radiation and sensible heat flux (Fig. S4), both of which are linked to the increased MSE—reflecting a warmer and wetter atmosphere. In comparison, during TD_LN2001, moisture convergence-induced precipitation changes were primarily concentrated between 50°S and 60°S (Fig. 4c). During TD_LN2023, the moisture convergence-induced precipitation increase along the coastal areas of Antarctica was further amplified by the steep coastal slopes through
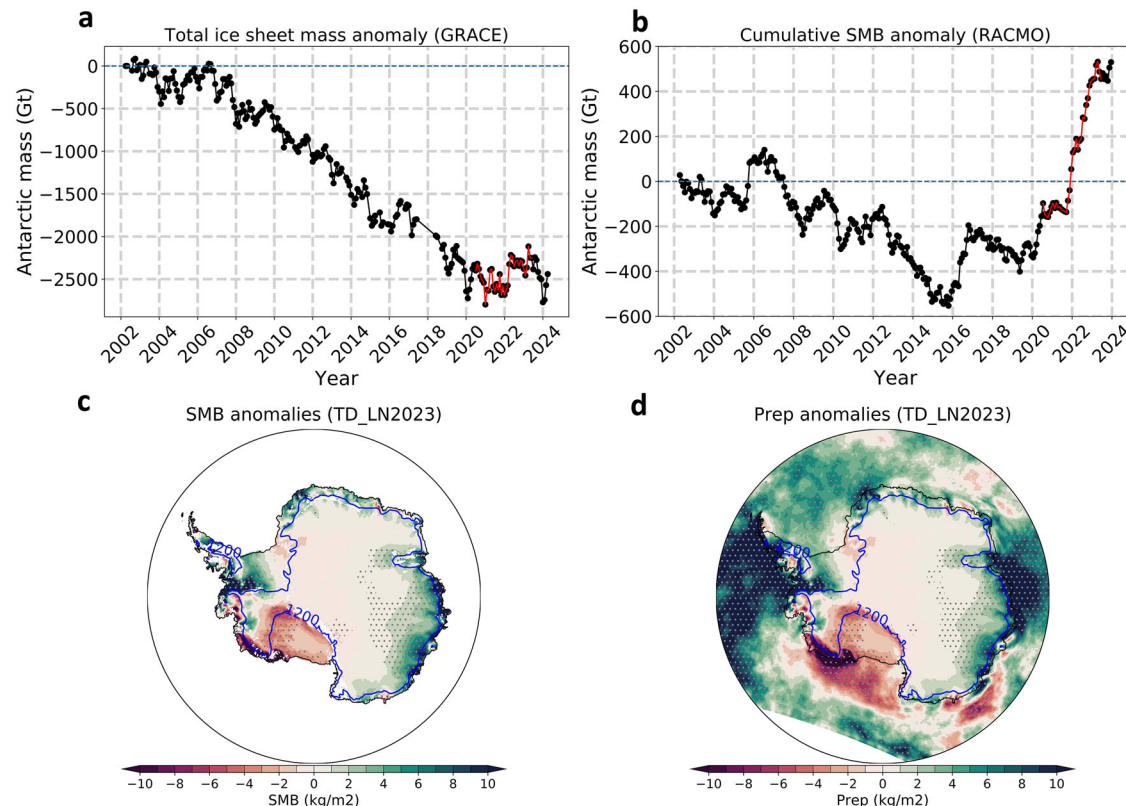
**Fig. 2 | Temporarily rebounded in Antarctic ice sheet masses and the surface mass balance changes during the recent triple-dip La Niña event. a** Timeseries of monthly Antarctic mass variation in Gt since April 2002, based on the Gravity Recovery and Climate Experiment (GRACE) data, with the period from July 2020 to June 2023 highlighted. **b** Timeseries of the cumulative surface mass balance (SMB) anomaly relative to April 2002, with the period from July 2020 to June 2023 highlighted. **c, d** Annual SMB and total precipitation (Prep) (from RACMO2.4P1) anomalies during 2021–2023, respectively. The dots indicate where the anomalies exceed one standard deviation ($1\sigma$) of the climatology (1991–2020). Blue lines denote the elevation of the Antarctic ice sheet at 1200 meters.

orographic lifting[26]. A detailed comparison between the TD_LN2023 and TD_LN2001 indicates that the southward shift of the Ferrel Cell during TD_LN2023 resulted in a corresponding shift of the MSE convergence zone (i.e., moisture and energy), leading to increased precipitation along the Antarctic coasts and a concurrent decrease in sea ice.

## Rossby wave train and stratosphere-troposphere coupling during 2021–2023

La Niña events tend to drive a southward shift of the Ferrel Cell[27,28]. Additionally, Rossby wave trains generated by La Niña events and emanating from the tropics serve as a key mechanism for horizontal teleconnections between the tropics and the Southern Hemisphere (SH) high-latitudes[20,29–32]. The cooling strengthens the polar vortex by increasing the temperature contrast between the cold polar air and warmer mid-latitudes[33]. A stronger polar vortex, in turn, influences the Antarctic surface climate in the following summer[34,35]. Generally, a stronger polar vortex descends into the troposphere, driving the positive phase of the SAM[34,36,37].

We begin by comparing the tropospheric circulation anomalies during the two TD_LN events. Compared to the TD_LN2001, the positive geopotential height (GPH) anomalies in TD_LN2023 were notably stronger, especially over the Amundsen-Bellingshausen Sea region (Fig. 5a, b), accompanied by a much deeper Amundsen Sea Low (ASL) (about −10 hPa during TD_LN2023) (Fig. 5c). The Rossby wave train induced by the TD_LN2023 also propagates eastward, generating positive GPH anomalies over the northern Weddell Sea, which extend southeastward toward the southern high-latitudes. This pattern demonstrates intensified teleconnections between the tropical Pacific and the SH high-latitudes. The stronger Rossby wave train is related to the southward shift of the Rossby wave source (Fig. 5b), accompanied by the southward shift of the regional Hadley Cell over the South Pacific and the South Pacific convergence zone (SPCZ) (Figs.

S5–6). The southward shift of the regional Hadley Cell and the SPCZ induces wind divergence in the upper troposphere, leading to a southward shift of the Rossby wave train (Fig. 5a, b). Additionally, a stronger mid-latitude westerly jet serves as a wave guide to navigate poleward and eastward propagation of the Rossby waves[19,38]. The deepening ASL (by approximately -4 hPa) corresponds with the elevated PSA pattern during TD_LN2023 (Fig. 5e).

Furthermore, there is a strong stratosphere-troposphere coupling during TD_LN2023 from austral spring through summer. The Antarctic stratosphere displayed significant cold anomalies (< −1 K) extending from 300 hPa to 10 hPa and the polar jet showed positive anomalies above 8 m/s, indicating a very deep and strong polar vortex (Fig. 6a). These anomalies are consistent with the anomalous Eliassen-Palm (E-P) fluxes—defined by upward E-P flux vectors that signify the upward propagation of planetary waves—which instead propagate downward from the stratosphere to the troposphere at 50°S to 70°S (Fig. 6a). The stronger westerly jet in the troposphere prevents the upward propagation of planetary waves[39] (Fig. 6a, c). During TD_LN2023, the polar vortex not only strengthened but also persisted longer (Fig. S7), with a delayed breakup due to its stability (Fig. 6a). During TD_LN2001, the polar vortex was also strong, but far weaker than that of TD_LN2023 (Fig. 6b, d). The prolonged polar vortex descended into the troposphere, enhancing the westerly jet and positive SAM from austral spring to summer[34,40]. The response in the troposphere showed that the strong PSA and ASL anomalies persist from austral spring to summer (Fig. 6c).

Antarctic sea ice anomalies are influenced by circulation anomalies through both thermodynamic and dynamical processes. The deepening of the ASL and elevated PSA pattern associated with the TD_LN2023 primarily induced robust northward sea ice motion, thereby promoting the formation of coastal polynyas over the Ross Sea (Fig. 1b). This process
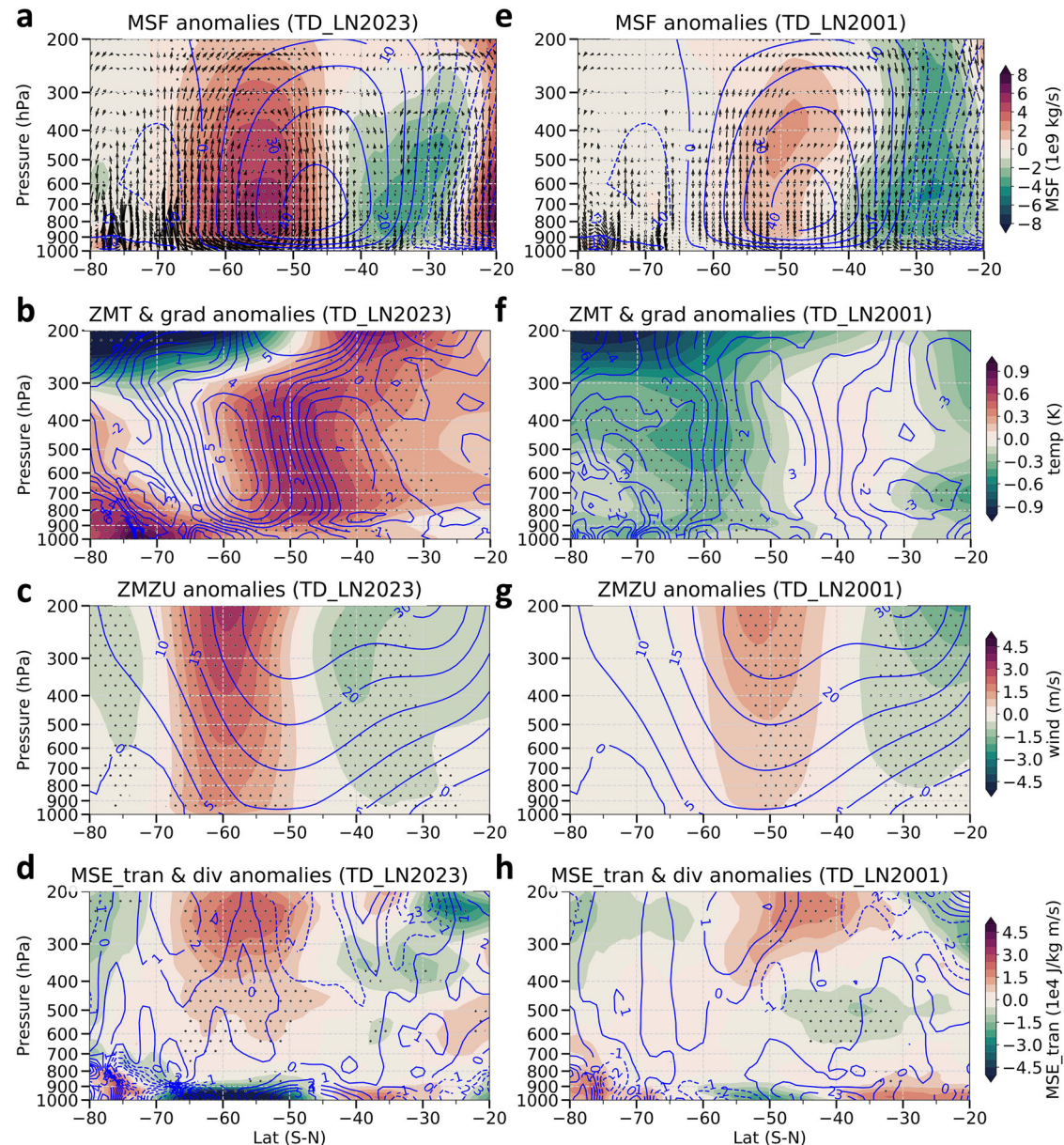
**Fig. 3 | Southward shift of the Ferrel Cell and the associated increases in temperature gradient, westerly jet and moist static energy transport. a** Annual meridional mass stream function (MSF) (shading) and wind vector anomalies. **b** Annual zonal mean temperature (ZMT) (shading) and meridional temperature gradient (contours; units: $1 \times 10^{-7}$ K/m). **c** Annual zonal mean zonal wind (ZMZU) (shading), and (**d**) Annual meridional moist static transport (MSE_tran) (shading) and its divergence (MSE_div) (contours; units: $1 \times 10^{-2}$ J/kg/s). Dot denotes that the anomalies exceeding $1\sigma$ of the climatology (1991–2020). The right panel (**e–h**) is the same as the left panel, but for circulation anomalies in TD_LN2001. Blue lines in (**a, e, c, g**) represent the climatological mean of MSF (units: $1 \times 10^9$ kg/s) and ZMZU (units: m/s), respectively.

contributes to sea ice loss through the ice-ocean albedo feedback[9]. Additionally, the deeper ASL and positive GPH anomalies over the northern Weddell Sea are linked to strong northwesterly-to-northerly wind anomalies, which transport warm and moist air masses from the north, leading to considerable loss of sea ice around the Antarctic Peninsula. Hence, the enhanced regional sea ice loss observed during TD_LN2023 could be partially attributed to the circulation anomalies induced by the TD_LN2023 event.

### Ekman Suction and Upper Ocean Warming during 2021–2023

The southward shift of the Ferrel Cell associated with La Niña events often leads to anomalous westerlies in high latitudes[28] (Fig. 3c). The circulation changes during TD_LN2023 also occurred under the background of intensified westerly winds and Southern Ocean warming, both of which

were driven by the increased emissions of $CO_2$ and ozone depleting substances[41,42]. Theoretically, the strengthened westerly winds or the positive phase of the SAM over the Southern Ocean lead to both the northward Ekman transport and Ekman upwelling. This process has been observed over the past four decades[4,41,43]. As discussed earlier, both the southward shift of the Ferrel Cell and enhanced stratosphere-troposphere coupling in TD_LN2023 contributed to the stronger and more persistent westerly anomalies and a positive SAM. The continued strengthening of westerly winds enhances Ekman upwelling (Fig. 7a–c). However, the actual impacts of the upwelling anomaly on the surface depends on the upper ocean thermal structure[44]. From Fig. 7d–f, we observe that before 2016, the vertical temperature structure of the Southern Ocean was characterized by surface cooling and subsurface warming according to the RG_ARGO (Roemmich-Gilson for Argo), ORAS5 (Ocean Reanalysis System 5), and IAPv4 (4th
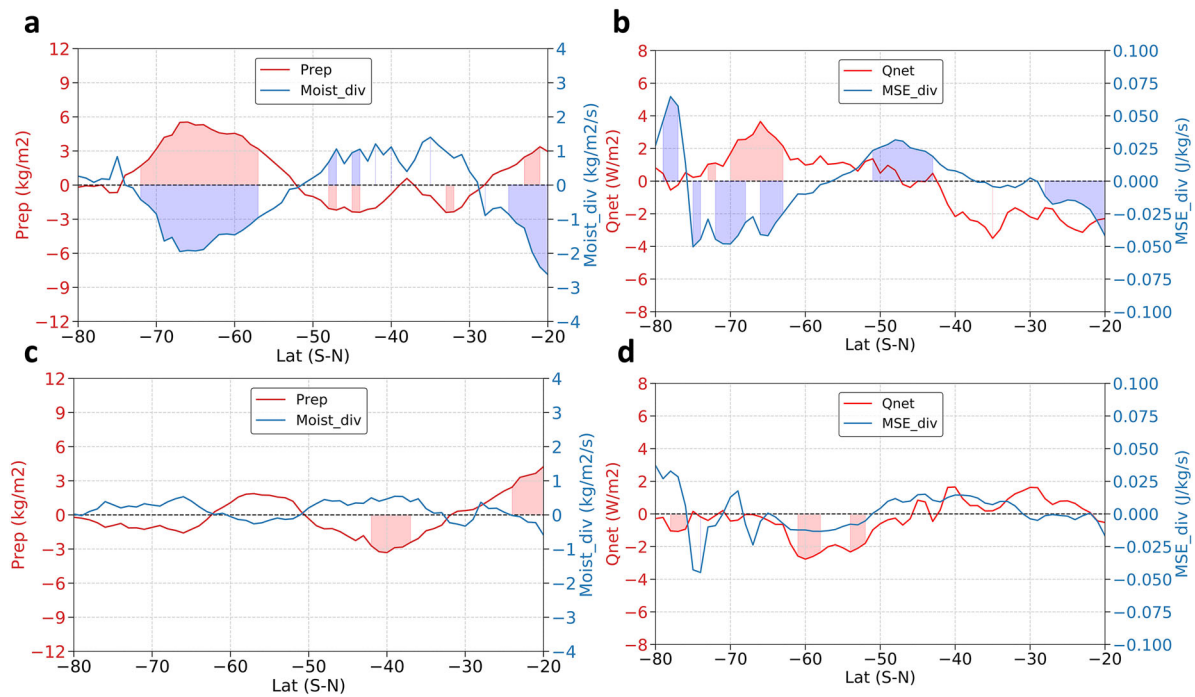
**Fig. 4 | Moisture and moist static energy convergence responsible for the high-latitude precipitation and sea ice changes. a** Annual zonal mean precipitation (Prep) (red line) and zonal mean moisture divergence (Moist_div) changes (blue line) during TD_LN2023. **b** Annual and zonal mean Qnet (red line) and moist static energy divergence (MSE_div) (blue line) changes, which are integrated from the surface to 800 hPa. **c, d** (the lower panel) are the same as the upper panel (**a, b**) but for TD_LN2001. Red and blue shadings indicate where the anomalies exceed 1σ of the climatology.
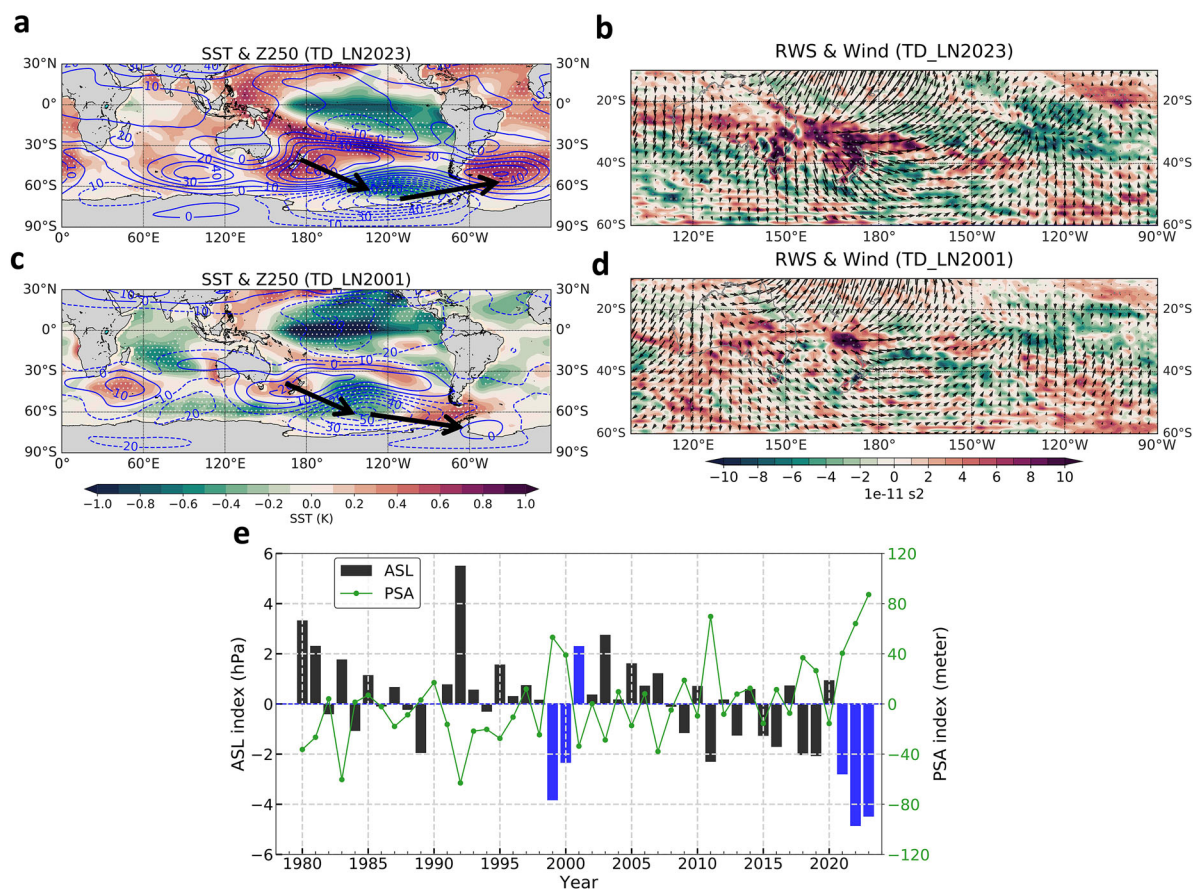


**Fig. 5 | A stronger Rossby wave train and the associated increases in the Pacific-South American Pattern. a** Annual geopotential height at 250 hPa (Z250) (contours; units: meter) and sea surface temperature (SST) (shading) anomalies during TD_2023. **b** Annual Rossby wave source (RWS) (shading) and irrotational component of wind vector anomalies at 250 hPa during TD_LN2023. **c, d** (the lower panel) are the same as the upper panel (**a, b**) but for TD_LN2001. **e** Timeseries of the annual ASL (**black bar**, TD_LN years are in blue) and PSA index (green line) from 1980 to 2023. Dot denotes that the SST and RWS anomalies exceed 1σ of the climatology (1991–2020).
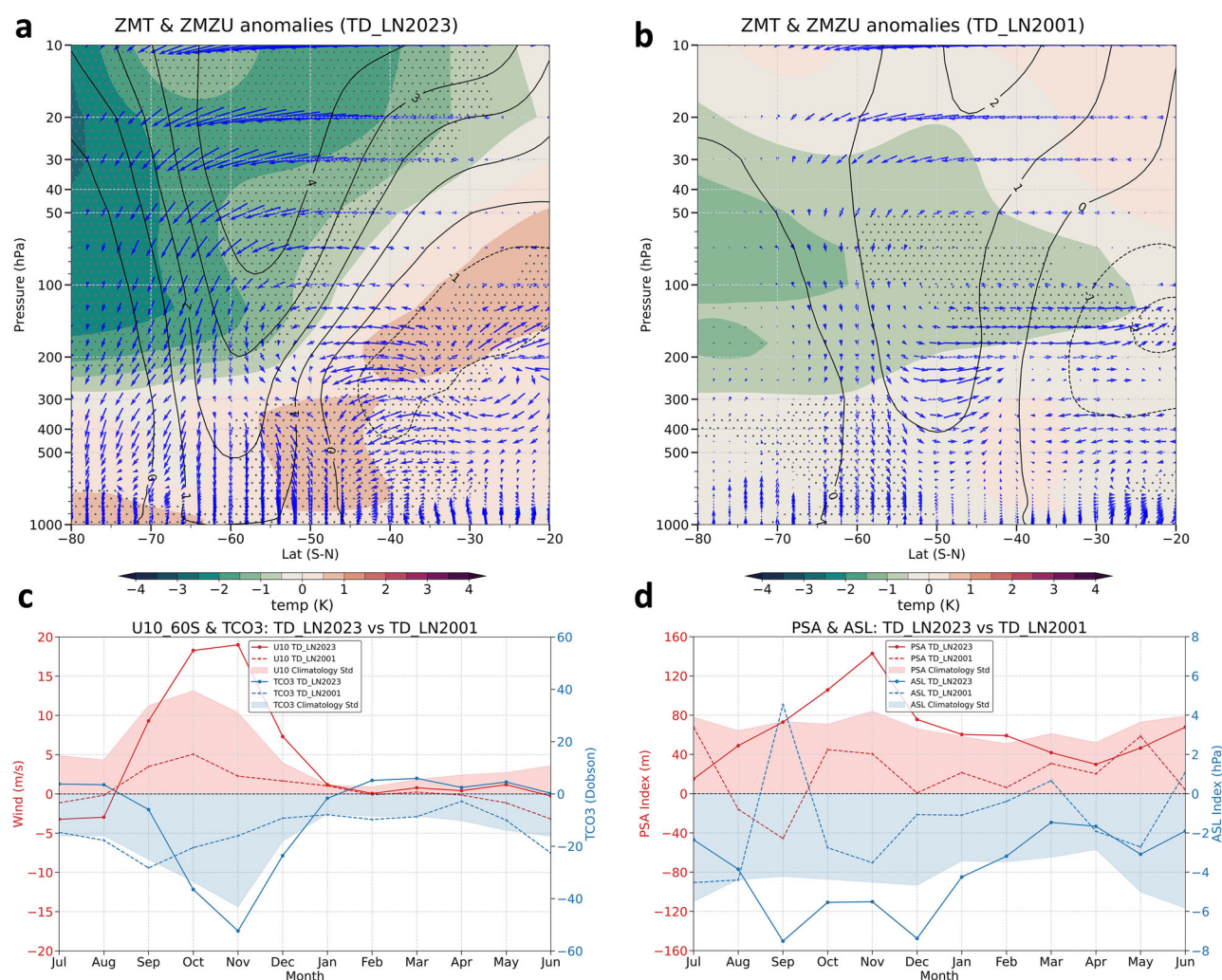
**Fig. 6 | A stronger stratosphere-troposphere coupling that sustains the PSA pattern from austral spring through summer. a** Annual zonal mean zonal wind (ZMZU) (contours; units: m/s) and zonal mean temperature (ZMT) (shading) anomalies, Eliassen-Palm (E-P) flux vector anomalies during TD_LN2023. **b** As in (**a**), but for anomalies during TD_LN2001. **c** Seasonal evolution of the ZMZU at 10 hPa and 60°S (U10_60S) (red lines) and the Antarctic total column ozone (TCO₃) (blue lines) during TD_LN2023 (solid lines) and TD_LN2001 (dashed lines). **d** As in (**c**), but for seasonal evolution of the PSA (red lines) and ASL (blue lines) index during TD_LN2023 (solid lines) and TD_LN2001 (dashed lines). Red and blue shadings in (**c**, **d**) represent 1σ of the climatology.

version of the Institute of Atmospheric Physics) datasets, consistent previous studies[6,45]. After 2016, following the transition to a new sea ice regime[6], three datasets consistently show that subsurface warming has been spreading upward, driven by enhanced Ekman suction. The change indicates a fundamental shift in ocean heat distribution. During TD_LN2023, the upward spreading of warm subsurface ocean water was seen from depths of 200–100 meters to approximately 50 meters (Fig. 7d–f, arrows). Furthermore, not only was the subsurface warming moving closer to the surface, but its intensity was also increasing over time. These two factors—upward spreading and increasing heat content—are key drivers of Antarctic sea ice loss.

**Relationship between the Southward Shift of the Ferrel cell and circulations**

As illustrated above, a key distinction between TD_LN2001 and TD_LN2023 lies in the position of the Ferrel Cell and the associated circulation anomalies. To further validate theses differences, we conduct empirical orthogonal function (EOF) analysis on the SH MSF (20°–80°S) to examine the longterm variations in the Ferrel Cell. Figure 8 presents the first two leading modes of the annual MSF from 1980 to 2023, which explain 51% and 20% of the total variance, respectively. EOF1 reflects the strengthening

of the Ferrel Cell, with the corresponding principal component (PC1) displaying a decadal enhancement since 1998, closely aligned with the tropical expansion (correlation coefficient = 0.77) (Fig. 8a, c). Meanwhile, the EOF2 captures the southward shift of the Ferrel Cell, centered around 50°S. The corresponding PC2 shows a strong annual enhancement from 2021 to 2023 (Fig. 8b, d), indicating a pronounced southward shift of the Ferrel Cell during TD_LN2023.

To demonstrate the connections between the southward shift of the Ferrel Cell and circulations, we conducted regression analysis between PC2 and the circulations (Fig. 9). A positive PC2, indicative of a southward shift of the Ferrel Cell, is associated with positive temperature anomalies in the mid-latitude troposphere, corresponding to the descent branch of the Ferrel Cell, while the Antarctic stratosphere exhibits significant cold anomalies (Fig. 9a). These anomalies closely align with observations (Fig. 6a). Similarly, the temperature patterns are consistent with a stronger stratospheric jet stream and an intensified mid-to-high latitude jet stream (Fig. 9b). Horizontally, a positive PC2 is linked to a PSA-like pattern with a significant deepening of the ASL (Fig. 9c). The southward shift of the westerlies also enhances the Ekman suction (Fig. 9d), facilitating upwelling of warm subsurface water. As a result, the circulation anomalies associated with a positive PC2 contribute to a substantial
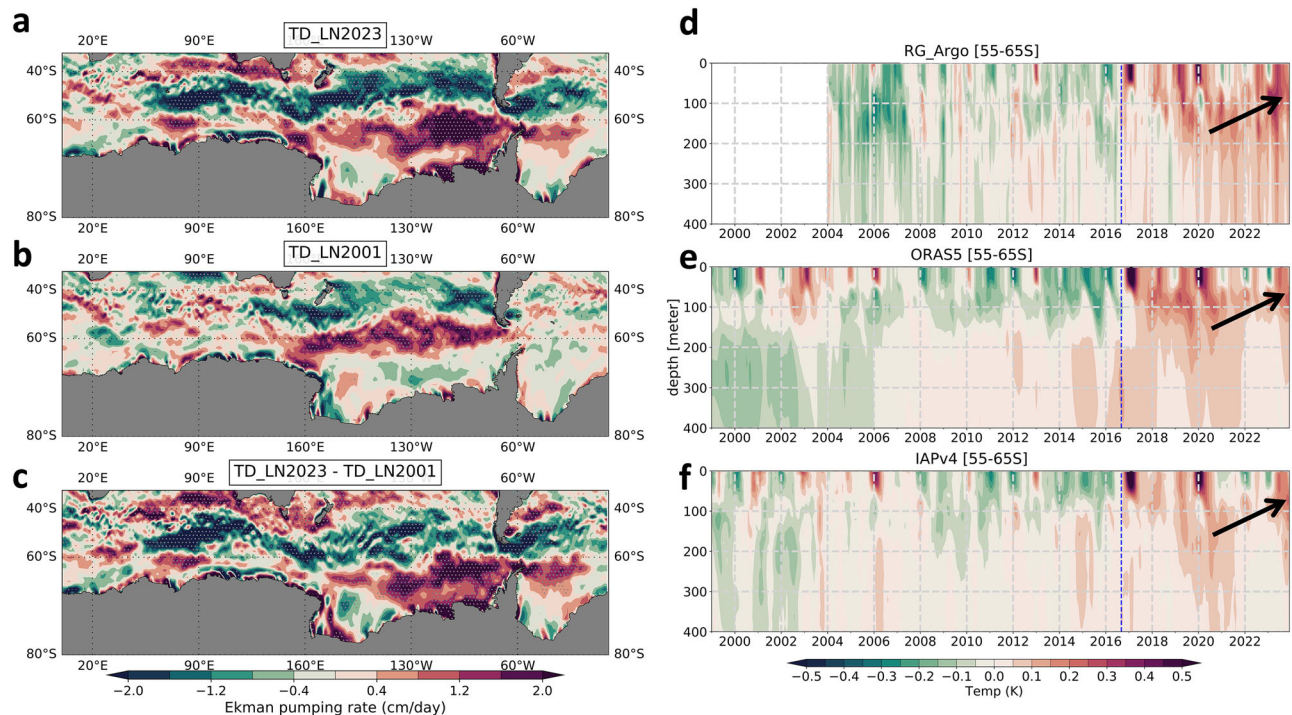
**Fig. 7 | Enhanced Ekman suction that facilitates subsurface warm water being transferred upward. a–c** Annual Ekman pumping rate anomalies during TD_LN2023, TD_LN2001, and their difference, respectively. Dots indicate that the anomalies/difference exceed $1\sigma$ of the climatology (1991–2020). **d–f** Evolution of the zonal mean ocean temperature anomalies (remove the longterm average) over the latitude band (55–65°S) based on RG_Argo, ORAS5, and IAPv4, respectively. Blue lines indicate the year 2016, marking the transition to new sea ice regime.

sea ice loss in the northern Weddell Sea, Ross Sea, and along the coastal regions of East Antarctica, while also driving a substantial increase in total precipitation over East Antarctica and the Antarctic Peninsula (Fig. 9e, f). Overall, these ice anomalies closely resemble the sea ice and SMB changes depicted in Figs. 1–2, further reinforcing the strong connection between the southward shift of the Ferrel Cell, regional sea ice retreat, and increased precipitation along the Antarctic coasts.

Compared to the circulation anomalies associated with PC2 (Figs. 9 vs. 10), the key distinction is that PC2 exhibits a zonally symmetric westerly jet strengthening, whereas PC1 is zonally asymmetric, linked to the deepening of the ASL, with westerly jet strengthening at the 50°–60°S and the increased precipitation north of 60°S in the Pacific sector. Clearly, the net impacts on Antarctic sea ice are distinctly different from those of PC2, which is related to a decrease in sea ice (Figs. 9e vs. 10e). Several previous studies have shown that a deepening ASL can lead to regional SIE expansion[17,29,46,47]. We also note that PC1 shows pronounced positive anomalies during TD_LN2001, which corresponds to a slightly increase in SIE, in contrast to the response observed during TD_LN2023. The physical connections between the southward shift of the Ferrel Cell and changes in Antarctic sea ice and ice sheet mass are further illustrated in Fig. 11.

## Discussion

We find that the enhanced tropical-Antarctic teleconnections during TD_LN2023 might have contributed to the dramatic changes in Antarctic sea ice and ice sheet, and their characteristics through the Ferrel Cell mechanism (Fig. 11). Compared to the previous TD_LN event, several factors contributed to the enhancement during TD_LN2023.

Firstly, although the difference in the Niño 3.4 index between the two TD_LN events is moderate (Fig. S2), the two events correspond to different responses of the Ferrel Cell—one involving strengthening and the other a southward shift (Fig. 3e vs. a). As shown in the regression analysis above, the strengthening of the Ferrel Cell (i.e., PC1) contributes to the expansion of the SIE, while the southward shift of the Ferrel Cell (i.e., PC2) leads to a

retreat of the SIE and ice sheet mass gain. This suggests that the mid-latitude responses to the TD_LN events are crucial in driving the contrasting effects on Antarctic sea ice.

Secondly, as demonstrated above, PC1 has shown a decadal enhancement since 1998. Positive PC1 is related to the increased westerly jet over the 50°–60°S latitude band and increased SST over the sub-tropical Pacific (Fig. 10b, c), indicating a southward shift of the SPCZ. The increase in the westerlies during TD_LN2023, superimposed on the positive tend linked to the decadal enhancement of the PC1, resulted in an enhanced Ekman suction and a stronger wave train. It is worth noting that both PC1 and PC2 exhibit strong correlations with the SAM, with coefficients of about 0.4 and 0.6, respectively (Fig. 8d). However, their net impacts on Antarctic sea ice are distinctly different (Figs. 9e vs. 10e). This study thus highlights a scenario in which La Niña events, particularly TD_LN, combined with the tropical expansion trend and stronger westerlies, contribute to warming in the high-latitude Southern Ocean, contrasting with the cooling effects reported in many previous studies[45,46,48]. The SIE retreat associated with TD_LN events is also consistent with findings based on the Coupled Model Intercomparison Project Phase 6 under a high-emission scenario[49].

Thirdly, around 2015/16, a transition in the Antarctic sea ice state occurred, shifting from a positive trend to a low level of SIE. The shift coincided with substantial warming of subsurface waters south of approximately 55°S and a significant increase in Southern Ocean heat content[50]. The Antarctic sea ice is more vulnerable for warmer subsurface water that is vertically advected by the enhanced Ekman suction.

Finally, ongoing anthropogenic global warming has amplified the effects of ENSO by increasing both atmospheric water vapor content and temperature[51]. Previous studies[27] have shown that both La Niña events and global warming can drive the southward shift of the Ferrel Cell. The strengthening of the Ferrel Cell further enhances the poleward transport of moist static energy from mid- to high- latitudes, contributing to pronounced sea ice loss and increased precipitation increase over the Antarctic coasts[23].
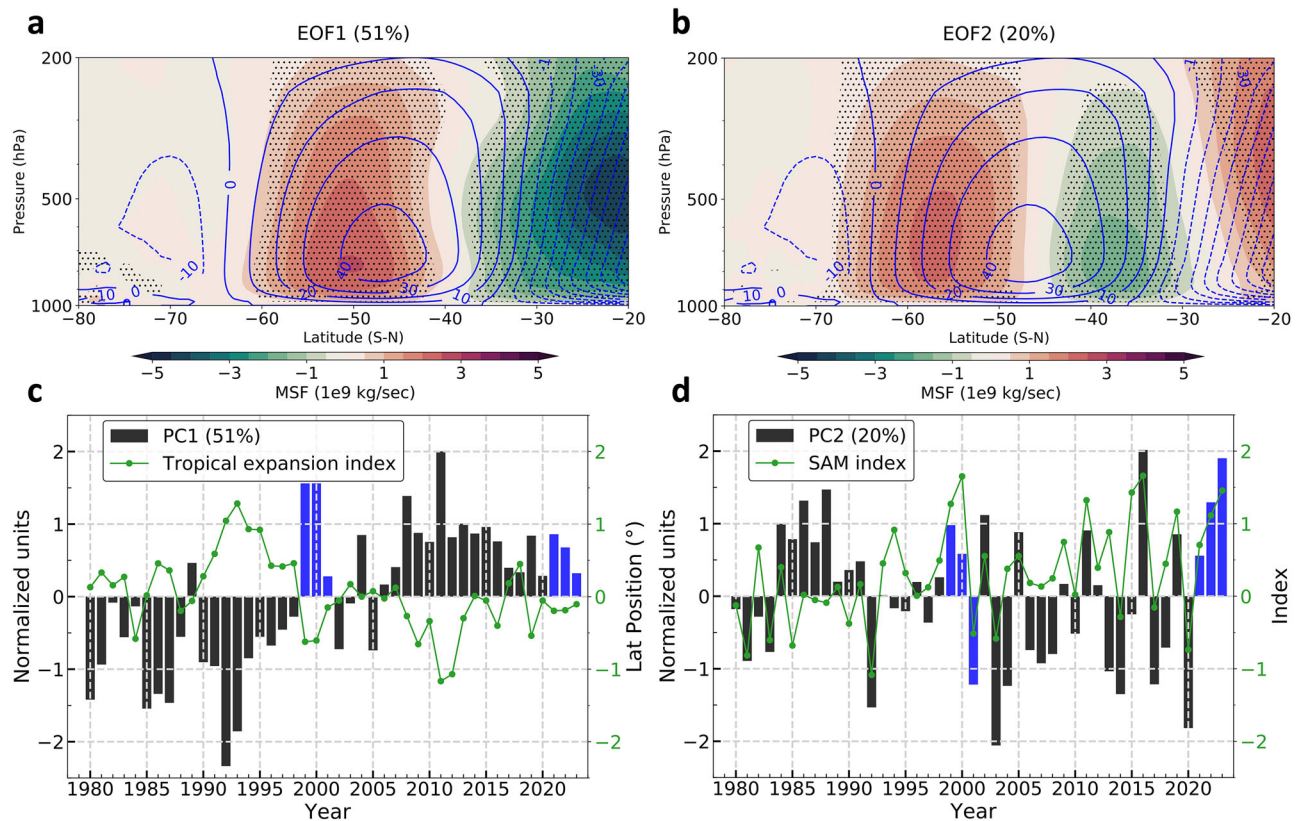
**Fig. 8 | Leading modes of the MSF of the Southern Hemisphere with the second mode corresponding to the southward shift of the Ferrel Cell. a**, **b** The first two leading modes of the annual MSF of the Southern Hemisphere (20–80°S) from 1980 to 2023. The explained variances are denoted in the brackets of the figure titles. Blue lines in a and b represent the climatological mean of MSF (units: $1 \times 10^9$ kg/s). **c** Timeseries of the first principal component (PC1) (black bar with TD_LN years in blue) and the annual tropical expansion index (green line) from 1980 to 2023. **d** Timeseries of the second principal component (PC2) (black bar with TD_LN years in blue) and the annual SAM index (green line) from 1980 to 2023.

Under global warming, multi-year La Niña events are projected to occur more frequently[52,53]. The tropical-Antarctic teleconnections introduce considerable internal variability and uncertainty into long-term predictions of the Antarctic surface climate. In this context, the responses of the mid-latitudes, particularly the Ferrel Cell, are of critical importance.

## Methods
### Data
The monthly sea ice concentration (SIC) for the period of 1979–2023 is obtained from the National Snow and Ice Data Center (NSIDC). This dataset is derived from the Nimbus-7 Scanning Multichannel Microwave Radiometer (SMMR), the Defense Meteorological Satellite Program (DMSP) Special Sensor Microwave Imager (SSM/I), and the DMSP Special Sensor Microwave Imager and Sounder (SSMIS) sensors using the NASA team algorithm[54]. The data are provided on the polar stereographic projection with a spatial resolution of 25 km. The SIE is defined as the total area of a pixel covered by at least 15% SIC.

The Global Sea Ice Concentration data set from the EUMETSAT Ocean and Sea Ice Satellite Application Facility (OSISAF) spans 1979 through the present. The data are generated using brightness temperature measurements from the Scanning Multichannel Microwave Radiometer (SMMR), the Special Sensor Microwave/Imager (SSM/I), and the Special Sensor Microwave Imager/Sounder (SSMIS) sensors aboard various Nimbus and Defense Meteorological Satellite Program (DMSP) satellites.

The monthly data of the ERA5 over the same period are used in this study[55], including mean sea level pressure (SLP), zonal and meridional winds, temperature, geopotential height, specific humidity, total precipitation (Prep), total column ozone ($TCO_3$) and surface heat fluxes.

Sea surface temperature (SST) data are obtained from the NOAA Extended Reconstructed Sea Surface Temperature V5 (ERSSTv.5) with a resolution of 2° × 2° and for the years 1979 to 2023[56]. When sea ice is present, the SST values are adjusted to the freezing temperature of seawater (−1.8 °C).

Ocean temperature data from 2004 to 2023 are derived from the extension of the gridded Argo data product as described in Roemmich and Gilson[57]. This product provides a 1° × 1° gridded atlas of monthly mean profiles for ocean temperature and salinity from the surface to 2000 dBar (hPa), based on data from Argo profiling floats. While this dataset does not include shipboard measurements, it provides broad spatial coverage of the Southern Ocean within a homogenous dataset.

The ocean temperature data are from the ocean and sea-ice reanalyses (ORAs, or ocean syntheses) of version 5 (ORAS5), which is a global eddy-permitting ocean and sea-ice ensemble reanalysis[58].

Additionally, ocean temperature and ocean heat content (OHC) data are obtained from the 4th version of the Institute of Atmospheric Physics (IAPv4) objective analysis product[59].

RACMO2.4P1 data set includes the surface mass balance (SMB) components, surface energy budget variables and near-surface climate variables as is simulated by the regional atmospheric climate model RAC-MO2.4p1 over Antarctica from January 1979 to December 2023[60].

### Climate indices
Sea ice extent (SIE) is defined as the total area covered by at least 15% sea ice concentration (SIC). The Niño 3.4 index is the area-averaged SST anomaly from 5°S–5°N in latitude and 170°E–120°W in longitude.
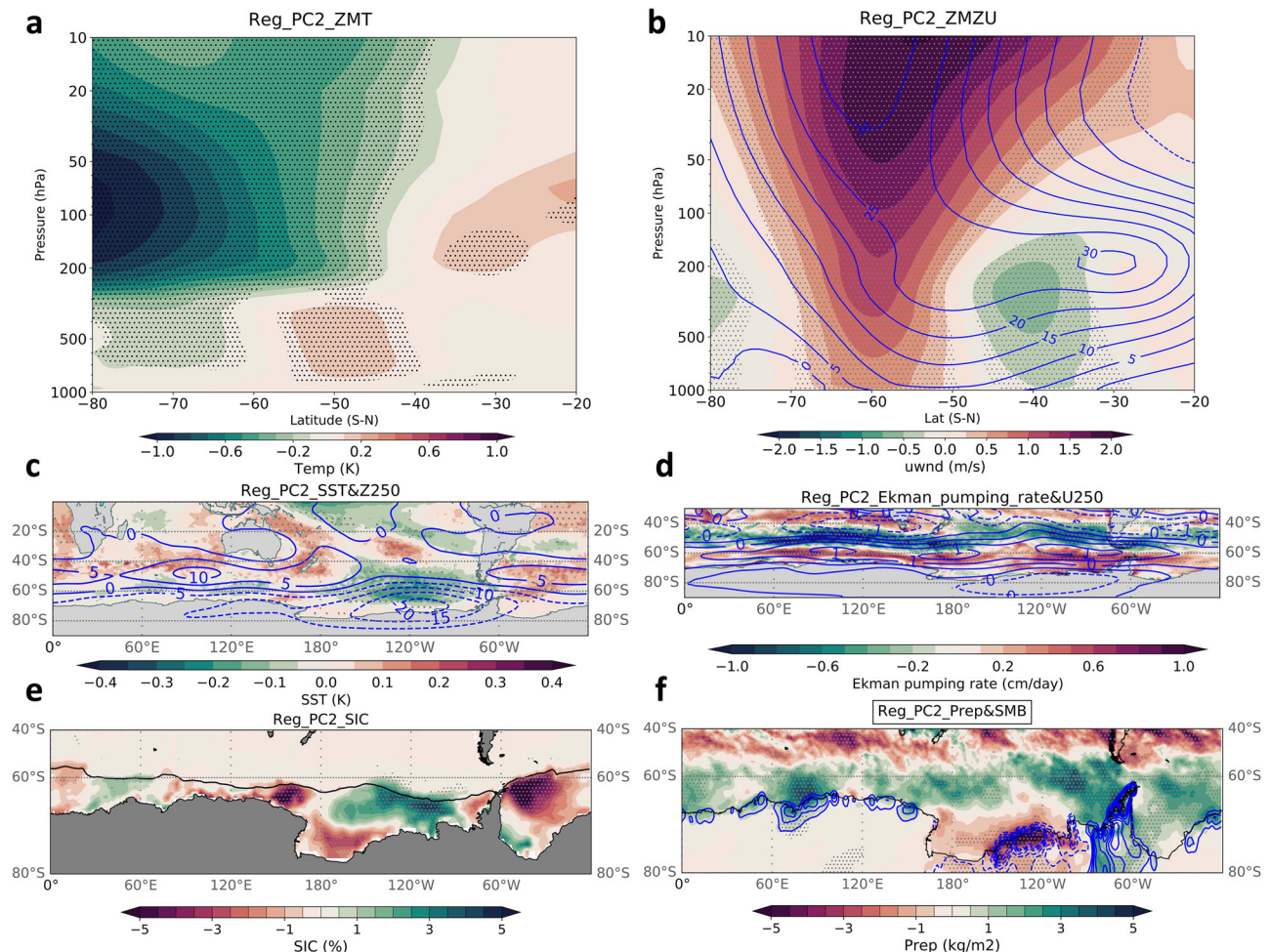
**Fig. 9 | Southward shift of the Ferrel Cell and the associated changes in circulations, sea ice and SMB. a–f** Regression coefficients between the second principal component (PC2) and annual mean key variables over 1980–2023: (**a**) Zonal mean temperature (ZMT), (**b**) Zonal mean zonal wind (ZMZU), (**c**) sea surface temperature (SST, shading) and geopotential height at 250 hPa (Z250, contours; meter), (**d**) Ekman pumping rate (shading) and zonal wind at 250 hPa (U250, contours; m/s), (**e**) sea ice concentration (SIC), and (**f**), precipitation (Prep, shading) and surface mass balance (SMB, contours; kg/m²). Dots denote the regression coefficients significant at 95% confidence level. Black line in **e** represents the climatological sea ice edges (15% SIC).

The strength of the stratospheric polar vortex in the SH is computed as the zonal mean zonal wind at 10 hPa and 60°S (U10_60S).

The Southern Annular Mode (SAM), which is the dominant mode of middle-to-high latitude climate variability. Here, the SAM index is defined as the difference in zonal mean SLP between 40°S and 65°S[61].

The ASL index is defined as the area-averaged SLP within the domain of 170°E to 298°E in longitude and 60°S to 80°S in latitude[62].

The Pacific South American (PSA) pattern is characterized by a stationary Rossby wave train originating from the tropical central Pacific, with major anomaly centers located to the east of New Zealand, in the Amundsen–Bellingshausen Seas, and near the southern tip of South America. Following the Yuan and Li[63], the PSA pattern index is defined by monthly geopotential height (GPH) anomalies at 250 hPa (Z250) at three anomalous centers: to the east of New Zealand, in the Amundsen Sea, and in the Southwest Atlantic. This definition is expressed as:

$$PSA = \frac{H1 + H2 - H3}{3}$$

Here, we use Z250 values at the following coordinates for H1, H2, and H3, respectively: 45°W, 50°S; 170°W, 45°S; and 120°W, 67.5°S.

Polar vortex breakup date is defined as the transition from westerlies to easterlies at 10 hPa and 60°S (U10_60S)[64].

The Southern Hemisphere Hadley Cell edge is used to indicate the tropical expansion, which is defined as the latitude where the mean meridional MSF reaches zero at 500 hPa of the Southern Hemisphere[65].

## Mass stream function (MSF)
The strength of the Ferrel Cell is measured by the mean meridional MSF[66], which is calculated as

$$MSF = \frac{2\pi a \cos\phi}{g} \int_p^{Ps} v(p, \phi) \, dp$$

where $a$, $\phi$, $p$ and $v$ denote Earth's radius, latitude, atmospheric pressure, zonal mean meridional wind, respectively.

## MSE and its poleward transport and divergence
The MSE is calculated as the summation of three terms and are shown below:

$$MSE = c_p T + L_v q + gz$$

$C_p$ denotes the specific heat at constant pressure, $L_v$ denotes latent heat of vaporization, and $g$, $z$ are the gravitational constant and the geopotential height, respectively. The meridional transport of the MSE is defined as the
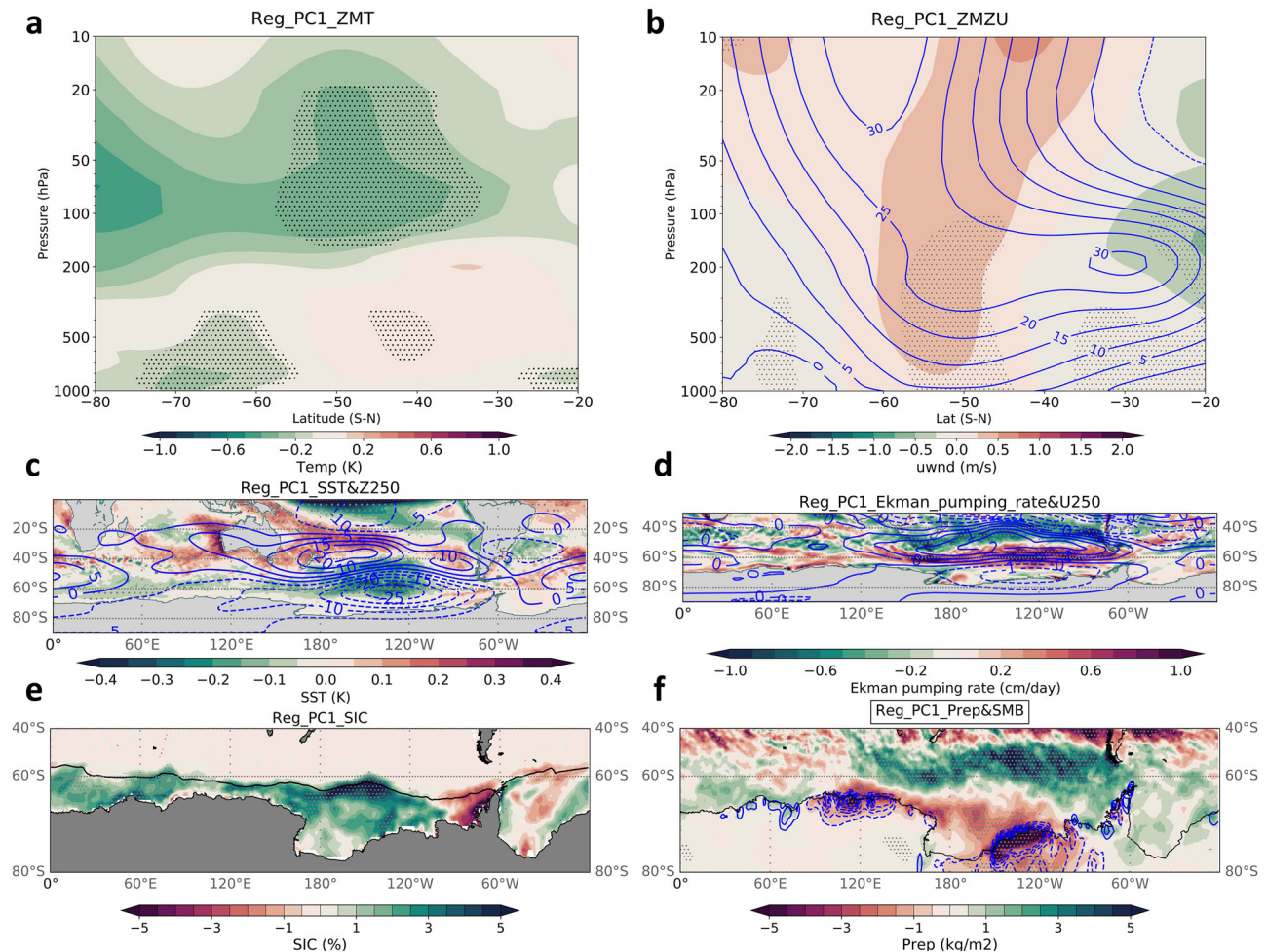
**Fig. 10 | Strengthening of the Ferrel Cell and the associated changes in circulations, sea ice and SMB. a–f** Regression coefficients between the first principal component (PC1) and annual mean key variables over 1980–2023: (**a**) zonal mean temperature (ZMT), (**b**) zonal mean zonal wind (ZMZU), (**c**) Sea surface temperature (SST, shading) and geopotential height at 250 hPa (Z250, contours; meter). **d** Ekman pumping rate (shading) and zonal wind at 250 hPa (U250, contours; m/s), (**e**) Sea ice concentration (SIC), and (**f**) precipitation (Prep, shading) and surface mass balance (SMB, contours; kg/m²). Dots denote the regression coefficients significant at 95% confidence level. Black line in (**e**) represents the climatological sea ice edges (15% SIC).

mathematical product of the meridional wind (v) and MSE. The formula is shown below:

$$MSE\ transport = vMSE$$

The meridional divergence of the MSE transport is defined below,

$$MSE\ divergence = \frac{\partial(vMSE)}{\partial y}$$

**Net surface heat flux (Qnet)**
Qnet is calculated as the summation of the net surface radiative fluxes and turbulent heat fluxes and are shown below:

$$Qnet = Qlw + Qsw + Qlat + Qsen$$

$Qlw$, $Qsw$, $Qlat$, and $Qsen$ denote the net longwave radiation, net shortwave radiation, latent heat flux and sensible heat flux, respectively. By convention, the surface fluxes are positive downward.

**Eliassen-Palm (E-P) flux vector**
We use E-P flux to diagnose planetary wave activities and subsequently wave-mean flow interaction, which is one of the major mechanisms of the stratosphere-troposphere coupling. Following the textbook[67], in log-pressure coordinate, the EP flux is defined as

$$\left[F_\varnothing, F_p\right] = \rho_0 a \cos\varnothing \left[-\overline{u'v'}, \frac{\overline{v'\theta'}}{\partial\bar{\theta}/\partial z}f\right]$$

where $\rho_0$, $f$ and $a$ are air density, the Coriolis parameter and the Earth's radius; z and $\varnothing$ are log-pressure height and latitude; the $\bar{\theta}$ is the zonal mean potential temperature, and $\overline{u'v'}$, $\overline{v'\theta'}$ are the vertical eddy heat the momentum fluxes. Following linear theory, upward E-P flux vectors indicate that planetary waves propagate upward and an E-P flux convergence above indicates that breaking planetary waves are exerting a drag on the mean flow causing a deceleration of the mean flow. **Rossby Wave Source (RWS).** The RWS is defined as in Sardeshmukh and Hoskins[68],

$$RWS = \nabla \cdot V_x(f + \zeta)$$

**Fig. 11 | Schematic illustration of the connections between the tropical triple-dip La Niña events and Antarctic surface climate changes through the southward shift of the Ferrel Cell.** The diagram illustrates the southward shift of the Ferrel Cell (green arrows), which drives the southward advection of heat and moisture (red arrows) (contributing to sea ice decrease), and shifts rainfall southward (supporting ice sheet mass increase). This shift also strengthens the westerly jet (large arrow), sustained by enhanced stratosphere–troposphere coupling. Changes of westerly jet further intensify Ekman suction (white arrows) (promoting additional sea ice loss). Horizontally, the shift is linked to an intensified Pacific–South American (PSA) pattern (brown circles) (contributing to regional sea ice decrease). The enhanced tropical–Antarctic teleconnections during TD_LN2023 occurred against the background of tropical expansion (dark blue arrow).
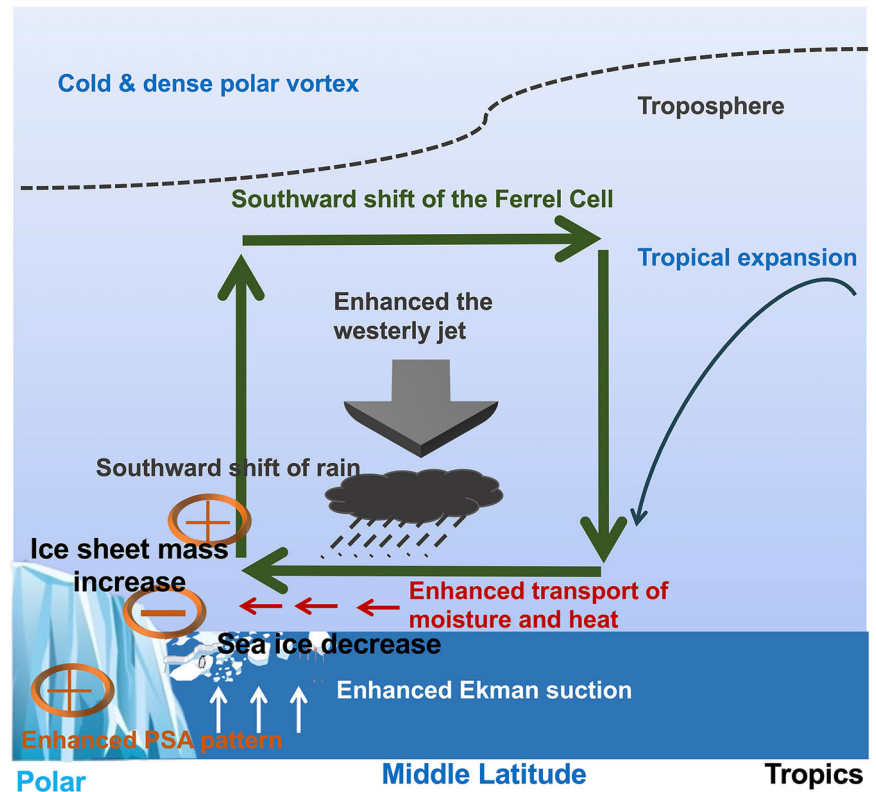


where $V_x$ denotes the divergent wind velocity, $f$ and $\zeta$ denote the Coriolis parameter and the relative vorticity, respectively.

**Ekman pumping rate**

Ekman pumping rate induced vertical velocity is calculated as follows,

$$wE = \text{curl}(\boldsymbol{\tau}_s/\rho f) = \frac{\partial}{\partial x}\left(\frac{\tau_{ys}}{\rho f}\right) + \frac{\partial}{\partial y}\left(-\frac{\tau_{xs}}{\rho f}\right)$$

where $\tau_s$ is the surface wind stress vector $(\tau_{xs}, \tau_{ys})$, $f$ is the Coriolis parameter and $\rho$ is the density of seawater, approximated here as 1025 kg m$^{-3}$.

**Data availability**

All the data analyzed here are openly available. ERA5, https://cds.climate.copernicus.eu/datasets/reanalysis-era5-pressure-levels-monthly-means?tab=download. MERRA2, https://gmao.gsfc.nasa.gov/reanalysis/MERRA-2/. NSIDC sea ice, https://noaadata.apps.nsidc.org/NOAA/G02202_V4/south/. OSISAF sea ice, https://doi.org/10.15770/EUM_SAF_OSI_0008. ERSSTv.5, https://psl.noaa.gov/data/gridded/data.noaa.ersst.v5.html. RG_ARGO, https://sio-argo.ucsd.edu/RG_Climatology.html. ORAS5, https://cds.climate.copernicus.eu/datasets/reanalysis-oras5?tab=download. IAPv4, http://www.ocean.iap.ac.cn/. RACMO2.4p1, https://zenodo.org/records/14217232. The SAM, https://legacy.bas.ac.uk/met/gjma/sam.html. GRACE data, https://climate.nasa.gov/vital-signs/ice-sheets/?intent=121.

**Code availability**

The codes to calculate results associated with main figures in this study are available upon request.

**References**

1. Turner, J. et al. Absence of 21st century warming on Antarctic Peninsula consistent with natural variability. *Nature* **535**, 411–415 (2016).
2. Hobbs, W. R. et al. A review of recent changes in Southern Ocean sea ice, their drivers and forcings. *Glob. Planet. Change* **143**, 228–250 (2016).
3. Parkinson, C. L. A 40-y record reveals gradual Antarctic sea ice increases followed by decreases at rates far exceeding the rates seen in the Arctic. *Proc. Natl Acad. Sci.* **116**, 14414–14423 (2019).
4. Armour, K. C., Marshall, J., Scott, J. R., Donohoe, A. & Newsom, E. R. Southern Ocean warming delayed by circumpolar upwelling and equatorward transport. *Nat. Geosci.* **9**, 549–554 (2016).
5. Liu, J., Zhu, Z. & Chen, D. Lowest Antarctic sea ice record broken for the second year in a row. *Ocean-Land-Atmos. Res.* **2**, 0007 (2023).
6. Purich, A. & Doddridge, E. W. Record low Antarctic sea ice coverage indicates a new sea ice state. *Commun. Earth Environ.* **4**, 314 (2023).
7. Wille, J. D. et al. The Extraordinary March 2022 East Antarctica "Heat" Wave. Part I: Observations and Meteorological Drivers. *J. Clim.* **37**, 757–778 (2024).
8. Wang, W., Shen, Y., Chen, Q. & Wang, F. Unprecedented mass gain over the Antarctic ice sheet between 2021 and 2022 caused by large precipitation anomalies. *Environ. Res. Lett.* **18**, 124012 (2023).
9. Wang, S. et al. Contribution of the deepened Amundsen sea low to the record low Antarctic sea ice extent in February 2022. *Environ. Res. Lett.* **18**, 054002 (2023).
10. Rignot, E. et al. Four decades of Antarctic Ice Sheet mass balance from 1979–2017. *Proc. Natl Acad. Sci.* **116**, 1095–1103 (2019).
11. Yang, T. et al. Mass Balance of the Antarctic Ice Sheet in the Early 21st Century. *Remote Sens.* **15**, 1677 (2023).

12. Miles, B. W. J. et al. High spatial and temporal variability in Antarctic ice discharge linked to ice shelf buttressing and bed geometry. *Sci. Rep.* **12**, 10968 (2022).

13. Gardner, A. S. et al. Increased West Antarctic and unchanged East Antarctic ice discharge over the last 7 years. *Cryosphere* **12**, 521–547 (2018).

14. Wang, Y., Wu, Q., Zhang, X. & Zhai, Z. Record-breaking Antarctic snowfall in 2022 delays global sea level rise. *Sci. Bull.* **68**, 3154–3157 (2023).

15. Yang, D. et al. Role of Tropical Variability in Driving Decadal Shifts in the Southern Hemisphere Summertime Eddy-Driven Jet. *J. Clim.* **33**, 5445–5463 (2020).

16. Ding, Q., Steig, E. J., Battisti, D. S. & Küttel, M. Winter warming in West Antarctica caused by central tropical Pacific warming. *Nat. Geosci.* **4**, 398–403 (2011).

17. Purich, A. et al. Tropical Pacific SST Drivers of Recent Antarctic Sea Ice Trends. *J. Clim.* **29**, 8931–8948 (2016).

18. Li, X., Holland, D. M., Gerber, E. P. & Yoo, C. Impacts of the north and tropical Atlantic Ocean on the Antarctic Peninsula and sea ice. *Nature* **505**, 538–542 (2014).

19. Karoly, D. J. & Hoskins, B. J. Three Dimensional Propagation of Planetary Waves. *J. Meteorological Soc. Jpn. Ser. II* **60**, 109–123 (1982).

20. Yuan, X., Kaplan, M. R. & Cane, M. A. The Interconnected Global Climate System—A Review of Tropical–Polar Teleconnections. *J. Clim.* **31**, 5765–5792 (2018).

21. Peixoto, J. P. & Oort, A. H. Physics of climate. (1992).

22. Liu, J. & Curry, J. A. Accelerated warming of the Southern Ocean and its impacts on the hydrological cycle and sea ice. *Proc. Natl Acad. Sci.* **107**, 14987–14992 (2010).

23. Wang, S. et al. How Has the Ferrel Cell Contributed to the Maintenance of Antarctic Sea Ice at Low Levels From 2016 to 2022? *Geophys. Res. Lett.* **51**, e2024GL108801 (2024).

24. Liu, J., Yuan, X., Rind, D. & Martinson, D. G. Mechanism study of the ENSO and southern high latitude climate teleconnections. *Geophys. Res. Lett.* **29**, 24-21–24-24 (2002).

25. Thompson, D. W. J. & Wallace, J. M. Annular Modes in the Extratropical Circulation. Part I: Month-to-Month Variability. *J. Clim.* **13**, 1000–1016 (2000).

26. Lenaerts, J. T. M., Medley, B., van den Broeke, M. R. & Wouters, B. Observing and Modeling Ice Sheet Surface Mass Balance. *Rev. Geophysics* **57**, 376–420 (2019).

27. Lu, J., Chen, G. & Frierson, D. M. W. Response of the Zonal Mean Atmospheric Circulation to El Niño versus Global Warming. *J. Clim.* **21**, 5835–5851 (2008).

28. Wang, G. et al. Future Southern Ocean warming linked to projected ENSO variability. *Nat. Clim. Change* **12**, 649–654 (2022).

29. Meehl, G. A., Arblaster, J. M., Bitz, C. M., Chung, C. T. & Teng, H. Antarctic sea-ice expansion between 2000 and 2014 driven by tropical Pacific decadal climate variability. *Nat. Geosci.* **9**, 590–595 (2016).

30. Ding, Q., Steig, E. J., Battisti, D. S. & Wallace, J. M. Influence of the Tropics on the Southern Annular Mode. *J. Clim.* **25**, 6330–6348 (2012).

31. Li, X. et al. Tropical teleconnection impacts on Antarctic climate changes. *Nat. Rev. Earth Environ.* **2**, 680–698 (2021).

32. Zhang, C., Li, S. & Han, Z. A Comparison of the Impacts of Two Consecutive Double-Peaked La Niña Events on Antarctic Sea Ice in Austral Spring. *J. Clim.* **37**, 3305–3321 (2024).

33. Domeisen, D. I. V., Garfinkel, C. I. & Butler, A. H. The Teleconnection of El Niño Southern Oscillation to the Stratosphere. *Rev. Geophysics* **57**, 5–47 (2019).

34. Lim, E.-P., Hendon, H. H. & Thompson, D. W. J. Seasonal Evolution of Stratosphere-Troposphere Coupling in the Southern Hemisphere and Implications for the Predictability of Surface Climate. *J. Geophys. Res.: Atmospheres* **123**, 12,002–012,016 (2018).

35. Sun, L., Chen, G. & Robinson, W. A. The Role of Stratospheric Polar Vortex Breakdown in Southern Hemisphere Climate Trends. *J. Atmos. Sci.* **71**, 2335–2353 (2014).

36. Thompson, D. W. J. et al. Signatures of the Antarctic ozone hole in Southern Hemisphere surface climate change. *Nat. Geosci.* **4**, 741–749 (2011).

37. Keeble, J., Braesicke, P., Abraham, N. L., Roscoe, H. K. & Pyle, J. A. The impact of polar stratospheric ozone loss on Southern Hemisphere stratospheric circulation and climate. *Atmos. Chem. Phys.* **14**, 13705–13717 (2014).

38. Karoly, D. J. Southern Hemisphere Circulation Features Associated with El Niño-Southern Oscillation Events. *J. Clim.* **2**, 1239–1252 (1989).

39. Charney, J. G. & Drazin, P. G. Propagation of planetary-scale disturbances from the lower into the upper atmosphere. *J. Geophys. Res. (1896-1977)* **66**, 83–109 (1961).

40. Byrne, N. J. & Shepherd, T. G. Seasonal Persistence of Circulation Anomalies in the Southern Hemisphere Stratosphere and Its Implications for the Troposphere. *J. Clim.* **31**, 3467–3483 (2018).

41. Cai, W. et al. Southern Ocean warming and its climatic impacts. *Sci. Bull.* **68**, 946–960 (2023).

42. Swart, N. C., Gille, S. T., Fyfe, J. C. & Gillett, N. P. Recent Southern Ocean warming and freshening driven by greenhouse gas emissions and ozone depletion. *Nat. Geosci.* **11**, 836–841 (2018).

43. Meehl, G. A. et al. Sustained ocean changes contributed to sudden Antarctic sea ice retreat in late 2016. *Nat. Commun.* **10**, 14 (2019).

44. Kostov, Y. et al. Fast and slow responses of Southern Ocean sea surface temperature to SAM in coupled climate models. *Clim. Dyn.* **48**, 1595–1609 (2017).

45. Fan, T., Deser, C. & Schneider, D. P. Recent Antarctic sea ice trends in the context of Southern Ocean surface climate variations since 1950. *Geophys. Res. Lett.* **41**, 2419–2426 (2014).

46. Chung, E.-S. et al. Antarctic sea-ice expansion and Southern Ocean cooling linked to tropical variability. *Nat. Clim. Change* **12**, 461–468 (2022).

47. Schneider, D. P. & Deser, C. Tropically driven and externally forced patterns of Antarctic sea ice change: reconciling observed and modeled trends. *Clim. Dyn.* **50**, 4599–4618 (2018).

48. Hu, Y., Tian, W., Dong, Y. & Zhang, J. Evaluating the Seasonal Responses of Southern Ocean Sea Surface Temperature to Southern Annular Mode in CMIP6 Models. *Geophys. Res. Lett.* **51**, e2024GL108782 (2024).

49. Cai, W. et al. Antarctic shelf ocean warming and sea ice melt affected by projected El Niño changes. *Nat. Clim. Change* **13**, 235–239 (2023).

50. Liu, J., Zhu, Z. & Chen, D. Lowest Antarctic Sea Ice Record Broken for the Second Year in a Row. *Ocean-Land-Atmos. Res.* **2**, https://doi.org/10.34133/olar.0007 (2023).

51. Hu, K., Huang, G., Huang, P., Kosaka, Y. & Xie, S.-P. Intensification of El Niño-induced atmospheric anomalies under greenhouse warming. *Nat. Geosci.* **14**, 377–382 (2021).

52. Geng, T. et al. Increased occurrences of consecutive La Niña events under global warming. *Nature* **619**, 774–781 (2023).

53. Wang, B. et al. Understanding the recent increase in multiyear La Niñas. *Nat. Clim. Change* **13**, 1075–1081 (2023).

54. Comiso, J. C., Meier, W. N. & Gersten, R. Variability and trends in the Arctic Sea ice cover: Results from different techniques. *J. Geophys. Res.: Oceans* **122**, 6883–6900 (2017).

55. Hersbach, H. et al. The ERA5 global reanalysis. *Q. J. R. Meteorol. Soc.* **146**, 1999–2049 (2020).

56. Huang, B. et al. Extended Reconstructed Sea Surface Temperature, Version 5 (ERSSTv5): Upgrades, Validations, and Intercomparisons. *J. Clim.* **30**, 8179–8205 (2017).

57. Roemmich, D. & Gilson, J. The 2004–2008 mean and annual cycle of temperature, salinity, and steric height in the global ocean from the Argo Program. *Prog. Oceanogr.* **82**, 81–100 (2009).

58. Zuo, H., Balmaseda, M. A., Tietsche, S., Mogensen, K. & Mayer, M. The ECMWF operational ensemble reanalysis–analysis system for ocean and sea ice: a description of the system and assessment. *Ocean Sci.* **15**, 779–808 (2019).

59. Cheng, L. et al. IAPv4 ocean temperature and ocean heat content gridded dataset. *Earth Syst. Sci. Data* **16**, 3517–3546 (2024).

60. van Dalum, C. T., van de Berg, W. J., van den Broeke, M. R. & van Tiggelen, M. The surface mass balance and near-surface climate of the Antarctic ice sheet in RACMO2.4p1. *EGUsphere* **2025**, 1–40 (2025).

61. Marshall, G. J. Trends in the Southern Annular Mode from Observations and Reanalyses. *J. Clim.* **16**, 4134–4143 (2003).

62. Hosking, J. S., Orr, A., Bracegirdle, T. J. & Turner, J. Future circulation changes off West Antarctica: Sensitivity of the Amundsen Sea Low to projected anthropogenic forcing. *Geophys. Res. Lett.* **43**, 367–376 (2016).

63. Yuan, X. & Li, C. Climate modes in southern high latitudes and their impacts on Antarctic sea ice. *J. Geophys. Res.: Oceans* **113**, https://doi.org/10.1029/2006JC004067 (2008).

64. Hurwitz, M. M. et al. Assessment of the breakup of the Antarctic polar vortex in two new chemistry-climate models. *J. Geophys. Res.: Atmos.* **115**, https://doi.org/10.1029/2009JD012788 (2010).

65. Staten, P. W., Lu, J., Grise, K. M., Davis, S. M. & Birner, T. Re-examining tropical expansion. *Nat. Clim. Change* **8**, 768–775 (2018).

66. Oort, A. H. & Yienger, J. J. Observed Interannual Variability in the Hadley Circulation and Its Connection to ENSO. *J. Clim.* **9**, 2751–2767 (1996).

67. Andrews, D. G., Leovy, C. B. & Holton, J. R. *Middle atmosphere dynamics*. (Academic press, 1987).

68. Sardeshmukh, P. D. & Hoskins, B. J. The Generation of Global Rotational Flow by Steady Idealized Tropical Divergence. *J. Atmos. Sci.* **45**, 1228–1251 (1988).

## Acknowledgements

## Author contributions

S.W. designed the study and wrote the initial manuscript in discussion with J.L., W.C. and S.D.; S.W. performed analysis and generated all figures. T.K. and X.C. helped to revise the manuscript. All authors contributed to interpreting the results and improving the paper.

## Competing interests

The authors declare no competing interests.

## Additional information

**Supplementary information** The online version contains supplementary material available at https://doi.org/10.1038/s41612-025-01066-0.

**Correspondence** and requests for materials should be addressed to Shaoyin Wang or Jiping Liu.

**Reprints and permissions information** is available at http://www.nature.com/reprints

**Publisher's note** Springer Nature remains neutral with regard to jurisdictional claims in published maps and institutional affiliations.